2011

Tethered Aerostat Modeling Using an Efficient Recursive Rigid-Body Dynamics Approach

Brad Hembree
University of Alabama - Huntsville

Nathan Slegers
George Fox University, nslegers@georgefox.edu

Tethered Aerostat Modeling Using an Efficient Recursive Rigid-Body Dynamics Approach

Brad Hembree* and Nathan Slegers†
University of Alabama in Huntsville, Huntsville, Alabama 35899

A tethered aerostat model is developed using a computationally efficient recursive tether model. The recursive rigid-body tether model results in unconstrained ordinary differential equations and maintains much of the simplicity of simple lumped-mass tether models, while avoiding numerical difficulties associated with using many stiff elastic elements with low mass. Further efficiency is achieved by treating each tether link as a body of revolution and assuming that tether spin is negligible to the dynamics. The tether is attached to a six-degree-of-freedom aerostat model using a single viscoelastic element. The final recursive tethered aerostat model is well suited for a variety of trade studies required for design and analysis of such systems, due to its low computational cost and numerical robustness. Simulations are used to show how the proposed recursive model can be used to investigate the dynamic response and tether loads for a 17 m tethered aerostat in response to varying winds.

Nomenclature

A, B, Q	=	apparent mass values
$\mathbf{a}_j^c$	=	acceleration of jth connection joint with respect to the inertial frame
$\mathbf{a}_j^m$	=	acceleration of mass center of jth link with respect to the inertial frame
b_j	=	jth link of the tether (ground link $j = 0$, root link $j = 1$, parent body $j = jp$)
C_{Dj}	=	tether drag coefficient
C_S	=	tether damping coefficient
C_v	=	viscous damping coefficient
c_j	=	jth connection joint (ground connection joint $j = 0$)
c_T	=	tether connection to aerostat
d	=	diameter of the tether
$\mathbf{E}_n$	=	$n \times n$ identity matrix
$\mathbf{F}_A, \mathbf{M}_A$	=	aerostat aerodynamic forces and moments
$\mathbf{F}_{\text{AM}}, \mathbf{M}_{\text{AM}}$	=	apparent mass force and moment
$\mathbf{F}_B$	=	aerostat buoyancy
$\mathbf{F}_{Dj}$	=	drag force for jth link
$\mathbf{F}_j$	=	5×1 force matrix for jth link
$\mathbf{F}_T, F_T$	=	viscoelastic element tension vector and magnitude
$\mathbf{F}_W$	=	aerostat weight
$\mathbf{I}_{\text{AM}}, \mathbf{I}_{\text{AI}}$	=	apparent mass and inertia matrices
$\mathbf{I}_B$	=	aerostat inertia matrix
$\mathbf{I}_j$	=	inertia matrix of jth body
$\tilde{\mathbf{I}}_j$	=	2×2 inertia matrix consisting of I_{yy} and I_{zz}
I_{nn}	=	mass moment of inertia about i, j, k body axes with $n = x, y, z$
$\mathbf{i}_B, \mathbf{j}_B, \mathbf{k}_B$	=	aerostat body-frame unit vectors
$\mathbf{i}_I, \mathbf{j}_I, \mathbf{k}_I$	=	inertial frame unit vectors
K_s, K_v	=	static and viscous stiffness
$\mathbf{L}_j$	=	moment in jth connection joint acting on the $(j+1)$th link and the jth link
$\tilde{\mathbf{L}}_j$	=	2×1 moment vector consisting of **j** and **k** components of $\mathbf{L}_j$
L_{nj}	=	nth component of $\mathbf{L}_j$ with $n = x, y, z$
L_{ve}	=	viscoelastic element unstretched length
$\bar{l}$	=	aerostat characteristic length
l_j	=	length of individual jth link
l_T	=	overall tether length
m_B	=	aerostat mass
m_{gas}	=	mass of aerostat gas
m_j	=	mass of link j
m_T	=	total mass of the tether
N	=	total number of tether links
p_B, q_B, r_B	=	aerostat angular velocity components
p_j, q_j, r_j	=	angular velocity components of the jth link
$\bar{q}$	=	aerostat dynamic pressure
$q_{0j}, q_{1j}, q_{2j}, q_{3j}$	=	quaternion parameters for jth link
$\mathbf{R}_j$	=	reaction in jth connection joint acting on the $(j+1)$th link and the jth links
$\mathbf{r}_j^c$	=	position vector from connection joint $j-1$ to connection joint j
$\mathbf{r}_{cg}^{cb}, \mathbf{r}_{cg}^{ct}$	=	position from the aerostat mass center to the center of buoyancy and c_T
$\mathbf{r}_j^m$	=	position vector from connection joint $j-1$ to mass center j
$\hat{\mathbf{S}}_j^c$	=	2×3 submatrix of skew-symmetric cross-product operator for position vector for $\mathbf{r}_j^c$
$\hat{\mathbf{S}}_j^m$	=	2×3 submatrix of skew-symmetric cross-product operator for position vector for $\mathbf{r}_j^m$
$\tilde{\mathbf{S}}_j^m$	=	2×2 submatrix for skew-symmetric cross-product operator for position vector $\mathbf{r}_j^m$
s_j	=	frontal area of jth link
s_{ve}	=	viscoelastic element stretch
$\mathbf{T}_I^B$	=	transformation from inertial to aerostat body frame
$\mathbf{T}_I^j$	=	transformation from inertial to jth body frame
$\mathbf{T}_{j-1}^j$	=	transformation from the $(j-1)$th body frame to the jth body frame
$\hat{\mathbf{T}}_{j-1}^j$	=	2×2 submatrix of the second and third columns of the second and third rows of $\mathbf{T}_{j-1}^j$
$\tilde{\mathbf{T}}_{j-1}^j$	=	1×2 submatrix of the second and third elements of the first row of $\mathbf{T}_{j-1}^j$
u, v, w	=	aerostat body velocity components
u_A, v_A, w_A	=	aerodynamic velocity components
$u_{\text{wind}}, v_{\text{wind}}, w_{\text{wind}}$	=	body-frame wind velocity components
Vol	=	aerostat volume

*Research Assistant, Mechanical and Aerospace Engineering.
†Assistant Professor, Mechanical and Aerospace Engineering. Member AIAA.

$\mathbf{V}_A$, V_A = aerodynamic velocity vector and magnitude
$\mathbf{V}_j$ = mass-center velocity of the jth link
$\dot{\mathbf{v}}_j$ = 5×1 acceleration vector consisting of components from $\tilde{\boldsymbol{\alpha}}_{j/I}$ and $\mathbf{a}^c_{j-1}$
$\mathbf{W}_j$ = weight of jth link
w_x, w_y, w_z = inertial frame wind components
x_{cj}, x_{mj} = length from $(j-1)$th connection to the jth connection and mass center
$\boldsymbol{\alpha}_{j/I}$ = angular acceleration vector of jth link with respect to the inertial frame
$\tilde{\boldsymbol{\alpha}}_{j/I}$ = 2×1 angular acceleration vector consisting of $\mathbf{j}$ and $\mathbf{k}$ components of $\boldsymbol{\alpha}_{j/I}$
Δx, Δy, Δz = viscoelastic element displacement
ϕ_B, θ_B, ψ_B = aerostat Euler angles
ϕ_j, θ_j, ψ_j = jth-link Euler angles
ρ_{air}, ρ_{gas} = atmospheric and aerostat gas density
ρ_j = appropriate density of air for jth-link drag calculations
$\boldsymbol{\omega}_B$ = aerostat angular velocity vector
$\dot{\boldsymbol{\omega}}_j$ = 2×1 angular acceleration vector consisting of the $\mathbf{j}$ and $\mathbf{k}$ components of $\dot{\boldsymbol{\omega}}_{j/j-1}$
$\boldsymbol{\omega}_{j/I}$ = angular velocity vector of jth link with respect to the inertial frame
$\boldsymbol{\omega}_{j/j-1}$ = relative angular velocity of jth link with respect to the $(j-1)$th link
$\tilde{\boldsymbol{\omega}}_{j/I}$ = 2×1 angular velocity vector consisting of $\mathbf{j}$ and $\mathbf{k}$ components of $\boldsymbol{\omega}_{j/I}$
ω_{nj} = nth component of $\boldsymbol{\omega}_{j/j-1}$ with $n = x, y, z$

I. Introduction

FINDING, tracking, and monitoring events and activities of interest on a continuous basis are critically important for intelligence, surveillance, and reconnaissance (ISR). In particular, it is desirable to monitor large areas of greater than 10 km^2 with either radar or high-resolution cameras for distinguishing and tracking people and vehicles. In addition, it is desirable to monitor these areas on a persistent basis using unmanned autonomous systems. Another key component in ISR is the communications-relay platform. Traditional mast-mounted antennas are limited in range and constrain the commander to available terrain. With a traditional mast-mounted antenna in typical terrain, about 2800 km^2 of battle space is covered. Line-of-sight coverage in the same terrain for an antenna at 300 m above ground level covers about 31,000 km^2: more than 10 times the mast-mounted antenna coverage.

Conventional tethered aerostats support both portions of ISR missions: providing high-resolution imagery to ground installations, and providing communications and data-relay to wide areas over any terrain. Unlike fixed-wing aircraft or helicopters, aerostats are lighter-than-air (typically using helium to stay aloft) and are tethered to the ground by a cable that also provides power. The most well established lighter-than-air program today is the Tethered Aerostat Radar System (TARS), which has been operating since 1980 at sites along the southern U.S. border. Each 71 m aerostat can lift radar or other sensors to a height of 3.5 km and can detect targets out to 500 km. The aerostat can theoretically stay aloft for days at a time and carries the AN/DPS-5 S-band and AN/TPS-63 search radar systems.

The Joint Land Attack Cruise-Missile-Defense Elevated Netted Sensor System (JLENS) uses the same 71 m TARS aerostat platform for the cruise-missile-defense radars being developed. Each JLENS system consists of two aerostats: one containing a broad-area surveillance radar to detect cruise missiles and the other a precision radar to track the cruise missile with sufficient precision to guide an intercepting weapon. Following initial threat detection by the surveillance radar, the precision radar takes over to generate a fire solution for available surface-to-air missiles. JLENS is seen by some as the centerpiece of a larger attempt to seamlessly link together numerous sensors across services to build a *single integrated air picture* that will enable effective cruise-missile defense. The U.S. Army has also deployed a 17 m Rapid Aerostat Initial Development (RAID) for Operation Enduring Freedom in 2001. The RAID system is essentially a much smaller version of JLENS (operating at approximately 300 m), has a payload of 90 kg, and provides short-range area surveillance and early warning against attacks with small arms, rockets, and mortars.

Modeling and analysis of airship dynamics has been growing, due to their potential use in a variety of areas such as low- and moderate-altitude applications previously explained, use as heavy-lift vehicles, and as a possible solution for near-space missions. Schmidt [1] investigated surge and directional dynamics of a high-altitude airship, while also investigating power required to stationkeep. Li and Nahon [2] proposed a modeling and estimation method for airships, then performed analysis based on a linearized version of the model and flight data. Lee and Bang [3] proposed a simplified airship model, later modified by Slegers and Brown [4], to design optimal trajectories for reaching altitude under hard constraints on trajectory boundaries. References [1–4] all consider aerostats which are not tethered, unlike TARS, JLENS, and RAID. Modeling of the coupled tethered aerostat system is crucial in analysis of such systems, because the large length of tether results in both the tether mass being a significant portion of the total mass and contributing additional drag. In addition, understanding and analyzing the coupled aerostat-tether dynamics is critical in design of the tether, aerostat, and payload.

Modeling of tethered aerostats has been proposed for a variety of systems, including 2-D analysis of aerostats in response to vertical gusts [5], tethered high-altitude balloons [6], and tritethered systems [7,8]. In all cases, the aerostat has a similar model that includes aerodynamics, buoyancy, and apparent mass whereas significantly different approaches are taken in modeling the tether. Although the tether is continuous, it is often modeled using discrete elements. The simplest aerostat-tether models use lumped-mass bodies connected with elastic elements [7,8] where each mass has only 3 degrees of freedom (DOF). A similar lumped-mass approach was used by Frost and Costello [9] when modeling connected munitions. A limitation of the simple lumped-mass model is that for stiff tethers, the elastic elements must also be stiff to mimic low strain, resulting in potentially high-frequency vibrations. Addition of a viscoelastic element in [10] improves performance of the lumped-mass model for stiff tethers while also adding an extra state for each viscoelastic element. Regardless of which element is used, elastic or viscoelastic, the lumped-mass models are appealing because they result in extremely simple, computationally efficient models, even for large numbers of elements. Tether modeling complexity is increased in [6], where beam elements are used rather than lumped masses. Using beam elements allows modeling of bending moments but requires a finite element nonlinear solver, and so the computational burden is much higher than the lumped-mass models. Similarly, [5] uses a more complex 2-D model, where tether elements are modeled as partial differential equations requiring an implicit finite difference algorithm coupled with a Newton–Raphson iterative scheme for a solution.

Tethered aerostats typically result in low tension in the tethers limited by the buoyancy. Often the tether is composed of a conductive core, either copper or aluminum, and a fiber optic cable. Strength of the tether is usually sufficient so that limitations in strain on fiber optics are not exceeded, resulting in the tether strain being small compared with the tether sway and surge. This paper models the tether using a chain of N bodies connected by spherical joints, rather than using stiff elastic elements and lumped masses. The proposed model results in unconstrained ordinary differential equations and maintains much of the simplicity of the lumped-mass models, while eliminating the numerical problems associated with extremely stiff elastic elements. The tether model takes the form of an open chain common to multibody dynamics, which can be solved using either an order-N^3 method by inverting a system mass matrix [11,12] or by recursive rigid-body dynamics, which is order N [13]. The later approach is taken here, because, as shown in [14], the order-N method is more computationally efficient as the number of bodies N increases. Computations are further decreased by treating each link as a body of revolution and assuming that tether spin is negligible to the dynamics, where each link then only has two degrees of freedom. The proposed recursive rigid-body tether formulation results in

computations on the same order as the three-degree-of-freedom lumped-mass models. Furthermore, elimination of high-stiffness elements allows larger integration time steps, further improving computation speeds. The efficient recursive tether model is coupled to the aerostat by a single viscoelastic element. The proposed efficient recursive tethered aerostat model is well suited for a variety of trade studies required for design and analysis due to its low computational cost and numerical robustness [15]. As a result, the proposed model can be considered a supplement to alternative approaches requiring an iterative scheme to solve partial differential equations [5] and a finite element nonlinear solver [6], for which the computational burden may be prohibitive when running large numbers of simulations for trade studies.

II. System Description

The tether is divided into N bodies connected by spherical joints with each link being a body of revolution. Figure 1 shows the tether attached to the ground with the jth body b_j having two connections: joints c_{j-1} and c_j. The Nth body b_N is the tether terminal link, body b_1 is the root link, where connection c_0 is stationary. Connection c_0 is attached to a fixed or inertial frame I defined by three orthogonal unit vectors: $\mathbf{i}_I$, $\mathbf{j}_I$, and $\mathbf{k}_I$. A link reference frame is assigned to each link, as shown with the origin at the link's mass center and $\mathbf{i}_j$ along the axis of revolution, with $\mathbf{j}_j$ and $\mathbf{k}_j$ defined to form an orthogonal triad. An aerostat body frame with unit vectors $\mathbf{i}_B$, $\mathbf{j}_B$, and $\mathbf{k}_B$ is located at the aerostat mass center, with $\mathbf{i}_B$ aligned with the aerostat's longitudinal axis and $\mathbf{k}_B$ in the vertical plane of symmetry. The aerostat and tether are connected by a single viscoelastic element from the aerostat harness connection c_T to tether terminal connection c_N.

Orientation of the aerostat is defined by a sequence of three body-fixed rotations. Starting from the inertial frame, the body frame is defined by rotations about the $\mathbf{k}$, $\mathbf{j}$, and $\mathbf{i}$ axes by angles ψ_B, θ_B, and ϕ_B, respectively, resulting in the transformation from the inertial frame I to the B frame:

$$\mathbf{T}_I^B = \begin{bmatrix} c_{\theta_B}c_{\psi_B} & c_{\theta_B}s_{\psi_B} & -s_{\theta_B} \\ s_{\phi_B}s_{\theta_B}c_{\psi_B} - c_{\phi_B}s_{\psi_B} & s_{\phi_B}s_{\theta_B}s_{\psi_B} + c_{\phi_B}c_{\psi_B} & s_{\phi_B}c_{\theta_B} \\ c_{\phi_B}s_{\theta_B}c_{\psi_B} + s_{\phi_B}s_{\psi_B} & c_{\phi_B}s_{\theta_B}s_{\psi_B} - s_{\phi_B}c_{\psi_B} & c_{\phi_B}c_{\theta_B} \end{bmatrix} \quad (1)$$

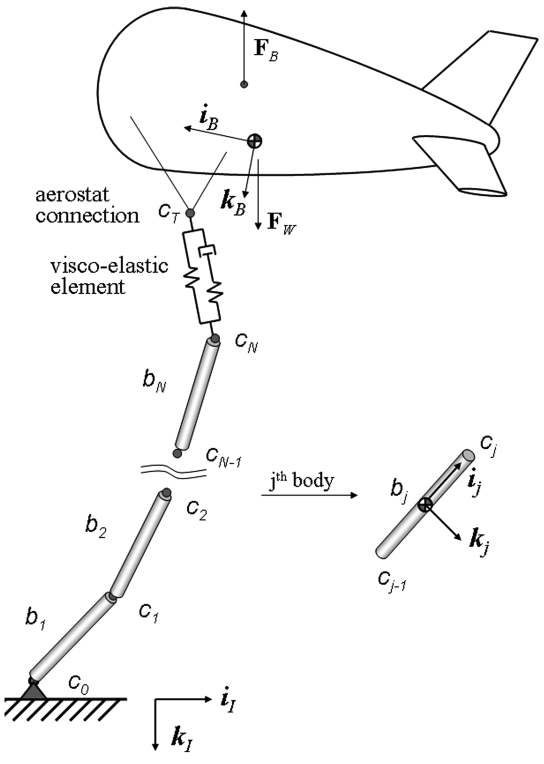

Fig. 1 Tethered aerostat schematic.

where $\sin(\chi) = s_\chi$, $\cos(\chi) = c_\chi$. Similarly, orientation of the jth-link frame is defined by a sequence of three body-fixed rotations, where the jth body frame is defined by rotations about the $\mathbf{k}$, $\mathbf{j}$, and $\mathbf{i}$ axes by angles ψ_j, θ_j, and ϕ_j, respectively. To avoid a singularity in the rotation kinematics, the link orientation can alternatively be defined by the four quaternion parameters (q_{0j}, q_{1j}, q_{2j}, and q_{3j}) [16], resulting in the transformation from the inertial frame I to the jth frame, given by

$$\mathbf{T}_I^j = \begin{bmatrix} 2q_{0j}^2 - 1 + 2q_{1j}^2 & 2q_{1j}q_{2j} + 2q_{0j}q_{3j} & 2q_{1j}q_{3j} - 2q_{0j}q_{2j} \\ 2q_{1j}q_{2j} - 2q_{0j}q_{3j} & 2q_{0j}^2 - 1 + 2q_{2j}^2 & 2q_{2j}q_{3j} + 2q_{0j}q_{1j} \\ 2q_{1j}q_{3j} + 2q_{0j}q_{2j} & 2q_{2j}q_{3j} - 2q_{0j}q_{1j} & 2q_{0j}^2 - 1 + 2q_{3j}^2 \end{bmatrix} \quad (2)$$

where

$$\begin{aligned} q_{0j} &= \cos\left(\frac{j}{2}\right)\cos\left(\frac{\theta_j}{2}\right)\cos\left(\frac{\phi_j}{2}\right) + \sin\left(\frac{j}{2}\right)\sin\left(\frac{\theta_j}{2}\right)\sin\left(\frac{\phi_j}{2}\right) \\ q_{1j} &= \cos\left(\frac{j}{2}\right)\cos\left(\frac{\theta_j}{2}\right)\sin\left(\frac{\phi_j}{2}\right) - \sin\left(\frac{j}{2}\right)\sin\left(\frac{\theta_j}{2}\right)\cos\left(\frac{\phi_j}{2}\right) \\ q_{2j} &= \cos\left(\frac{j}{2}\right)\sin\left(\frac{\theta_j}{2}\right)\cos\left(\frac{\phi_j}{2}\right) + \sin\left(\frac{j}{2}\right)\cos\left(\frac{\theta_j}{2}\right)\sin\left(\frac{\phi_j}{2}\right) \\ q_{3j} &= \sin\left(\frac{j}{2}\right)\cos\left(\frac{\theta_j}{2}\right)\cos\left(\frac{\phi_j}{2}\right) - \cos\left(\frac{j}{2}\right)\sin\left(\frac{\theta_j}{2}\right)\sin\left(\frac{\phi_j}{2}\right) \end{aligned} \quad (3)$$

A transformation from the $(j-1)$th frame to the jth frame can be formed using Eq. (2) and is given as

$$\mathbf{T}_{j-1}^{\,j} = (\mathbf{T}_j^I)^T \mathbf{T}_{j-1}^I \quad (4)$$

Position vectors from the $(j-1)$th connection to the jth body mass center are conveniently expressed in the b_j frame as $\mathbf{r}_j^m = x_{mj}\mathbf{i}_j$. Similarly, the vector from connection $j-1$ to connection j, also expressed in the b_j frame, is defined as $\mathbf{r}_j^c = x_{cj}\mathbf{i}_j$. Both vectors, $\mathbf{r}_j^m$ and $\mathbf{r}_j^c$, have only an $\mathbf{i}_j$ component as a result of each body's symmetry.

III. Aerostat Model

The aerostat is modeled as a rigid 6-DOF body, including three inertial positions of the aerostat mass center (x, y, and z) and the three Euler angles (ψ_B, θ_B, and ϕ_B). Body-frame velocity components of the aerostat mass center are u, v, w, and $\boldsymbol{\omega}_B$; the angular velocity of the aerostat (also in the body frame) has components p_B, q_B, and r_B. Forces and moments acting on the aerostat come from weight, buoyancy, aerodynamic loads, the viscoelastic connection from the aerostat harness to the tether, and apparent mass.

A. Aerostat Forces and Moments

Weight and buoyancy vectors, both expressed in the aerostat body frame, are written as

$$\mathbf{F}_W = \mathbf{T}_I^B \begin{Bmatrix} 0 \\ 0 \\ m_B g \end{Bmatrix} \quad (5)$$

$$\mathbf{F}_B = \mathbf{T}_I^B \begin{Bmatrix} 0 \\ 0 \\ -\mathrm{Vol}(\rho_{\mathrm{air}} - \rho_{\mathrm{gas}})g \end{Bmatrix} \quad (6)$$

where m_B is the aerostat mass excluding the enclosed-gas volume. Aerodynamic forces and moments take a standard form:

$$\mathbf{F}_A = \bar{q}\mathrm{Vol}^{2/3}\begin{Bmatrix} C_{A0} + C_{A2}\alpha^2 \\ C_{Y\beta}\beta \\ C_{N\alpha}\alpha \end{Bmatrix} \tag{7}$$

$$\mathbf{M}_A = \bar{q}\mathrm{Vol}^{2/3}\bar{l}\begin{Bmatrix} C_{l\beta}\beta + (\bar{l}/2V_A)C_{lp}p_B \\ C_{m0} + C_{m\alpha}\alpha + (\bar{l}/2V_A)C_{mq}q_B \\ C_{n\beta}\beta + (\bar{l}/2V_A)C_{nr}r_B \end{Bmatrix} \tag{8}$$

where $\bar{q}$ is the dynamic pressure, the characteristic length $\bar{l} = \mathrm{Vol}^{1/3}$, and V_A is the aerodynamic velocity magnitude. The aerodynamic velocity $\mathbf{V}_A = \{\, u_A \quad v_A \quad w_A \,\}^T$ is the difference of the aerostat body frame velocity and the wind velocity, also expressed in the body frame,

$$\begin{Bmatrix} u_A \\ v_A \\ w_A \end{Bmatrix} = \begin{Bmatrix} u \\ v \\ w \end{Bmatrix} - \begin{Bmatrix} u_{\text{wind}} \\ v_{\text{wind}} \\ w_{\text{wind}} \end{Bmatrix} \tag{9}$$

resulting in the aerodynamic angles being $\alpha = \tan^{-1}(w_A/u_A)$ and $\beta = \sin^{-1}(v_A/V_A)$.

B. Apparent Mass

Vehicles which displace a large mass of fluid compared with its own mass (such as aerostats, parachutes, and submarines) experience additional forces and moments, due to the fluid's acceleration. The forces and moments are often called *apparent mass*, because they appear as additional mass and inertia values in the final equations of motion. Similar to the results from [17,18], forces and moments from apparent mass are found by relating the fluid's kinetic energy to resultant forces and moments, resulting in

$$\mathbf{F}_{\text{AM}} = -\mathbf{I}_{\text{AM}}\begin{Bmatrix} \dot{u}_A \\ \dot{v}_A \\ \dot{w}_A \end{Bmatrix} - {}^B\mathbf{S}(\boldsymbol{\omega}_B)\mathbf{I}_{\text{AM}}\begin{Bmatrix} u_A \\ v_A \\ w_A \end{Bmatrix} \tag{10}$$

$$\mathbf{M}_{\text{AM}} = -\mathbf{I}_{\text{AI}}\begin{Bmatrix} \dot{p}_B \\ \dot{q}_B \\ \dot{r}_B \end{Bmatrix} - {}^B\mathbf{S}(\boldsymbol{\omega}_B)\mathbf{I}_{\text{AI}}\begin{Bmatrix} p_B \\ q_B \\ r_B \end{Bmatrix} \tag{11}$$

where the common convention is used that a cross-product of any vector $\mathbf{r}$ with components r_x, r_y, and r_z expressed in a frame C is written

$$\mathbf{r}\times = {}^C\mathbf{S}(\mathbf{r}) = \begin{bmatrix} 0 & -r_z & r_y \\ r_x & 0 & -r_x \\ -r_y & r_x & 0 \end{bmatrix} \tag{12}$$

Apparent mass and inertia matrices $\mathbf{I}_{\text{AM}}$ and $\mathbf{I}_{\text{AI}}$ in Eqs. (10) and (11) for an aerostat, which is approximately a body of revolution, can be written as diagonal matrices, where $\mathbf{I}_{\text{AM}} = \mathrm{diag}(A, B, B)$ and $\mathbf{I}_{\text{AI}} = \mathrm{diag}(0, Q, Q)$ with A, B, and Q being constants that are dependent on the aerostat geometry, which can be approximated according to [19]. Equation (10) can be expressed in terms of the aerostat body velocities and inertial winds w_x, w_y, and w_z by differentiation of Eq. (9) with respect to the aerostat body frame:

$$\mathbf{F}_{\text{AM}} = -\mathbf{I}_{\text{AM}}\left(\begin{Bmatrix} \dot{u} \\ \dot{v} \\ \dot{w} \end{Bmatrix} - \mathbf{T}_I^B\begin{Bmatrix} \dot{w}_x \\ \dot{w}_y \\ \dot{w}_z \end{Bmatrix}\right) + ({}^B\mathbf{S}(\boldsymbol{\omega}_B)\mathbf{I}_{\text{AM}} - \mathbf{I}_{\text{AM}}{}^B\mathbf{S}(\boldsymbol{\omega}_B))\mathbf{T}_I^B\begin{Bmatrix} w_x \\ w_y \\ w_z \end{Bmatrix} - {}^B\mathbf{S}(\boldsymbol{\omega}_B)\mathbf{I}_{\text{AM}}\begin{Bmatrix} u \\ v \\ w \end{Bmatrix} \tag{13}$$

C. Viscoelastic Link

The viscoelastic element connecting the aerostat and tether is composed of a spring with static stiffness K_s in parallel with a viscous spring of stiffness K_v and viscous damper with damping coefficient C_v. Viscoelastic line force is written in terms of components Δx, Δy, and Δz of the difference vector formed by subtracting the inertial position of the aerostat connection c_T and the tether connection c_N. Stretch of the viscoelastic element becomes $s_{\text{ve}} = \sqrt{\Delta x^2 + \Delta y^2 + \Delta z^2}$ and the stretch rate is $\dot{s}_{\text{ve}}$. Using the difference vector components, the line force vector is written as

$$\mathbf{F}_T = \frac{F_T}{s_{\text{ve}}}\begin{Bmatrix} \Delta x \\ \Delta y \\ \Delta z \end{Bmatrix} \tag{14}$$

Equation (15) provides the differential equation for the viscoelastic internal force F_T in terms of the stretch and stretch rate, and L_{ve} is the unstretched length:

$$\dot{F}_T + \frac{K_v}{C_v}F_T = \begin{cases} (K_v + K_s)\dot{s}_{\text{ve}} + \frac{K_vK_s}{C_v}(s_{\text{ve}} - L_{\text{ve}}), & s_{\text{ve}} - L_{\text{ve}} > 0 \\ 0 & s_{\text{ve}} - L_{\text{ve}} \le 0 \end{cases} \tag{15}$$

The first condition in Eq. (15) represents the viscoelastic element in tension, and the second represents the slack case, in which the internal force decays to zero.

D. Aerostat Dynamic Equations

Final dynamic equations of the aerostat are formed by equating the sum of external forces to the time derivative of linear momentum and equating the sum of moments about the aerostat mass center to the time derivative of angular momentum. Combining Eqs. (5–7), (11), (13), and (14) with the linear momentum derivative results in the following translation dynamic equations:

$$\begin{aligned}((m_B + m_{\text{gas}})\mathbf{E}_3 + \mathbf{I}_{\text{AM}})\begin{Bmatrix} \dot{u} \\ \dot{v} \\ \dot{w} \end{Bmatrix} &= \mathbf{F}_A + \mathbf{F}_W + \mathbf{F}_B - \mathbf{T}_I^B\mathbf{F}_T \\ &- {}^B\mathbf{S}(\boldsymbol{\omega}_B)((m + m_{\text{gas}})\mathbf{E}_3 + \mathbf{I}_{\text{AM}})\begin{Bmatrix} u \\ v \\ w \end{Bmatrix} + \mathbf{I}_{\text{AM}}\mathbf{T}_I^B\begin{Bmatrix} \dot{w}_x \\ \dot{w}_y \\ \dot{w}_z \end{Bmatrix} \\ &+ ({}^B\mathbf{S}(\boldsymbol{\omega}_B)\mathbf{I}_{\text{AM}} - \mathbf{I}_{\text{AM}}{}^B\mathbf{S}(\boldsymbol{\omega}_B))\mathbf{T}_I^B\begin{Bmatrix} w_x \\ w_y \\ w_z \end{Bmatrix}\end{aligned} \tag{16}$$

where $\mathbf{E}_3$ is a 3×3 identity matrix. Similarly, the rotational dynamics become

$$\begin{aligned}(\mathbf{I}_B + \mathbf{I}_{\text{AI}})\begin{Bmatrix} \dot{p}_B \\ \dot{q}_B \\ \dot{r}_B \end{Bmatrix} &= \mathbf{M}_A + {}^B\mathbf{S}(\mathbf{r}_{cg}^{cb})\mathbf{F}_B - {}^B\mathbf{S}(\mathbf{r}_{cg}^{ct})\mathbf{T}_I^B\mathbf{F}_T \\ &- {}^B\mathbf{S}(\boldsymbol{\omega}_B)(\mathbf{I}_B + \mathbf{I}_{\text{AI}})\begin{Bmatrix} p_B \\ q_B \\ r_B \end{Bmatrix}\end{aligned} \tag{17}$$

where $\mathbf{r}_{cg}^{cb}$ and $\mathbf{r}_{cg}^{ct}$ are the position vectors from the aerostat mass center to the center of buoyancy and aerostat connection, and $\mathbf{I}_B$ is the aerostat inertia matrix.

IV. Recursive Tether Model

The tether configuration in Fig. 1 has spherical joints connecting the N slender bodies with no applied twisting torque at the ground or terminal link. The combination results in the spin dynamics of each body having a minimal affect of the tether's overall motion. Elimination of tether spin will later aid in efficient computation of recursive dynamics. Angular velocity of the jth body with respect to the inertial frame of reference is then defined as

$$\boldsymbol{\omega}_{j/1} = q_j\mathbf{j}_j + r_j\mathbf{k}_j \tag{18}$$

where the spin rate p_j is zero. The angular velocity of the jth link, $\boldsymbol{\omega}_{j/I}$, may also be written as the sum of the previous body's angular velocity and the relative angular velocity of the jth link and its preceding link $\boldsymbol{\omega}_{j/j-1}$:

$$\boldsymbol{\omega}_{j/I} = \boldsymbol{\omega}_{j/j-1} + \mathbf{T}^j_{j-1}\boldsymbol{\omega}_{j-1/I} \tag{19}$$

with $\boldsymbol{\omega}_{j/j-1}$ expressed in the b_j frame. Equation (19) can equivalently be expressed in component form:

$$\boldsymbol{\omega}_{j/I} = \begin{Bmatrix} \omega_{xj} \\ \omega_{yj} \\ \omega_{zj} \end{Bmatrix} + \mathbf{T}^j_{j-1}\begin{Bmatrix} 0 \\ q_{j-1} \\ r_{j-1} \end{Bmatrix} = \begin{Bmatrix} 0 \\ q_j \\ r_j \end{Bmatrix} \tag{20}$$

where ω_{xj}, ω_{yj}, and ω_{zj} are the components of the relative angular velocity $\boldsymbol{\omega}_{j/j-1}$. Equation (20) can be separated into two portions: first, the requirement that

$$\omega_{xj} = -\tilde{\mathbf{T}}^j_{j-1}\begin{Bmatrix} q_{j-1} \\ r_{j-1} \end{Bmatrix} \tag{21}$$

where $\tilde{\mathbf{T}}^j_{j-1}$ is a 1×2 submatrix formed from the second and third elements of the first row of $\mathbf{T}^j_{j-1}$, and second,

$$\tilde{\boldsymbol{\omega}}_{j/I} = \begin{Bmatrix} \omega_{yj} \\ \omega_{zj} \end{Bmatrix} + \hat{\mathbf{T}}^j_{j-1}\begin{Bmatrix} q_{j-1} \\ r_{j-1} \end{Bmatrix} = \begin{Bmatrix} q_j \\ r_j \end{Bmatrix} \tag{22}$$

where $\hat{\mathbf{T}}^j_{j-1}$ is a 2×2 submatrix formed from the second and third columns of the second and third rows of $\mathbf{T}^j_{j-1}$. A special case occurs at the root link b_1, because for the ground b_0, both q_0 and r_0 are zero, so that $\omega_{x1} = 0$ and

$$\tilde{\boldsymbol{\omega}}_{1/I} = \begin{Bmatrix} \omega_{y1} \\ \omega_{z1} \end{Bmatrix} = \begin{Bmatrix} q_1 \\ r_1 \end{Bmatrix} \tag{23}$$

Differentiation of the angular velocity with respect to the inertial frame results in the angular acceleration of the jth body, taking the recursive form:

$$\boldsymbol{\alpha}_{j/I} = \dot{\boldsymbol{\omega}}_{j/j-1} + \boldsymbol{\omega}_{j/I} \times \boldsymbol{\omega}_{j/j-1} + \mathbf{T}^j_{j-1}\boldsymbol{\alpha}_{j-1/I} \tag{24}$$

where $\dot{\boldsymbol{\omega}}_{j/j-1}$ is the angular acceleration of b_j with respect to b_{j-1} expressed in the b_j frame. Expansion of Eq. (24) into matrix form results in

$$\boldsymbol{\alpha}_{j/I} = \begin{Bmatrix} 0 \\ \dot{q}_j \\ \dot{r}_j \end{Bmatrix} = \begin{Bmatrix} \dot{\omega}_{xj} \\ \dot{\omega}_{yj} \\ \dot{\omega}_{zj} \end{Bmatrix} + \begin{Bmatrix} -r_j\omega_{yj} + q_j\omega_{zj} \\ r_j\omega_{xj} \\ -q_j\omega_{xj} \end{Bmatrix} + \mathbf{T}^j_{j-1}\begin{Bmatrix} 0 \\ \dot{q}_{j-1} \\ \dot{r}_{j-1} \end{Bmatrix} \tag{25}$$

The first row of Eq. (25) is automatically satisfied by Eq. (21). Substitution of Eq. (21) into the remaining two equations results in

$$\tilde{\boldsymbol{\alpha}}_{j/I} = \begin{Bmatrix} \dot{q}_j \\ \dot{r}_j \end{Bmatrix} = \begin{Bmatrix} \dot{\omega}_{yj} \\ \dot{\omega}_{zj} \end{Bmatrix} - \begin{Bmatrix} r_j \\ -q_j \end{Bmatrix}\tilde{\mathbf{T}}^j_{j-1}\begin{Bmatrix} q_{j-1} \\ r_{j-1} \end{Bmatrix} + \hat{\mathbf{T}}^j_{j-1}\begin{Bmatrix} \dot{q}_{j-1} \\ \dot{r}_{j-1} \end{Bmatrix} \tag{26}$$

which can be written compactly as

$$\tilde{\boldsymbol{\alpha}}_{j/I} = \dot{\boldsymbol{\omega}}_j + \boldsymbol{\lambda}_j + \hat{\mathbf{T}}^j_{j-1}\tilde{\boldsymbol{\alpha}}_{j-1/I} \tag{27}$$

$$\boldsymbol{\lambda}_j = \begin{Bmatrix} r_j \\ -q_j \end{Bmatrix}\tilde{\mathbf{T}}^j_{j-1}\begin{Bmatrix} q_{j-1} \\ r_{j-1} \end{Bmatrix} \tag{28}$$

where $\dot{\boldsymbol{\omega}}_j = \{\, \dot{\omega}_{yj} \quad \dot{\omega}_{zj} \,\}^T$.

Acceleration of the jth body's mass center $\mathbf{a}^m_j$ and acceleration of the jth connection joint $\mathbf{a}^c_j$ for $j = 0$ to $N-1$ can be written in the b_j frame as

$$\mathbf{a}^{\,m}_j = \mathbf{T}^j_{j-1}\mathbf{a}^c_{j-1} + \boldsymbol{\alpha}_{j/I} \times \mathbf{r}^m_j + \boldsymbol{\omega}_{j/I} \times (\boldsymbol{\omega}_{j/I} \times \mathbf{r}^m_j) \tag{29}$$

$$\mathbf{a}^{\,c}_j = \mathbf{T}^j_{j-1}\mathbf{a}^c_{j-1} - \mathbf{r}^c_j \times \boldsymbol{\alpha}_{j/I} + \boldsymbol{\omega}_{j/I} \times (\boldsymbol{\omega}_{j/I} \times \mathbf{r}^c_j) \tag{30}$$

where it is noted that $\mathbf{a}^c_0 = 0$, since joint zero is attached to the ground.

The angular acceleration components of b_j in Eq. (27) and acceleration of the $(j-1)$th joint equation (30) can be combined into a 5×1 acceleration vector $\dot{\mathbf{v}}_j = \{\, \tilde{\boldsymbol{\alpha}}_{j/I} \quad \mathbf{a}^c_{j-1} \,\}^T$ and written

$$\dot{\mathbf{v}}_j = \mathbf{D}_j\dot{\mathbf{v}}_{j-1} + \mathbf{G}_j\dot{\boldsymbol{\omega}}_j + \boldsymbol{\Lambda}_j \tag{31}$$

where

$$\mathbf{D}_j = \begin{bmatrix} \hat{\mathbf{T}}^j_{j-1} & 0 \\ (\hat{\mathbf{S}}^c_j)^T & \mathbf{T}^{j-1}_{j-2} \end{bmatrix}, \qquad \mathbf{G}_j = \begin{bmatrix} \mathbf{E}_2 \\ 0 \end{bmatrix} \tag{32}$$

$$\boldsymbol{\Lambda}_j = \begin{bmatrix} \boldsymbol{\lambda}_j \\ \boldsymbol{\omega}_{j-1/I} \times (\boldsymbol{\omega}_{j-1/I} \times \mathbf{r}^c_{j-1}) \end{bmatrix}, \qquad \hat{\mathbf{S}}^c_j = \begin{bmatrix} 0 & 0 & -x_{cj} \\ 0 & x_{cj} & 0 \end{bmatrix} \tag{33}$$

A. Terminal Body Recursive Dynamics

The necessary dynamic equations for the tether model are formed using a Newtonian approach. A total of $2N$ vector equations are assembled, and these equations will consist of N force equations and N moment equations. Forces on each body include weight $\mathbf{W}_j$ and an external force $\mathbf{F}_{Dj}$, associated with it; both are defined in the inertial frame. In addition, a reaction force -$\mathbf{R}_j$ on body b_j, defined in the b_j frame, occurs at the jth joint for all j except for the terminal body. An equal-but-opposite reaction $\mathbf{R}_j$ is present on body b_{j+1}. A moment- $\mathbf{L}_j$ on body b_j, also defined in the b_j frame, occurs at the jth joint for all j except for the terminal body. An equal-but-opposite moment $\mathbf{L}_j$ is also present on body b_{j+1}. Neglecting spin dynamics requires that the moment $\mathbf{L}_j$ cannot impart a twisting moment; i.e., internal joint moments originate only from relative link bending and bending rates. The terminal link also has an external load $\mathbf{F}_T$ from the viscoelastic element applied at the end of the terminal body. Formation of the dynamic equations is achieved by summing forces and moments for individual links, with the moment equation expressed in the j body frame and the force equation expressed in the $(j-1)$th body frame. The two vector equations can then be put in a recursive form, where moving through the tether from the terminal link back toward the root link, equations for the $(j-1)$th links contain terms from the jth link such that these relationships become coupled. The recursive dynamic equations are developed below, first for a terminal link then for a nonterminal link.

Equating the time derivative of linear momentum with the summation of forces in the $(j-1)$th body frame for a terminal link j results in

$$\mathbf{R}_{j-1} + \mathbf{T}^{j-1}_I(\mathbf{F}_{Dj} + \mathbf{W}_j + \mathbf{F}_T) = m_j(\mathbf{T}^j_{j-1})^T\mathbf{a}^m_j \tag{34}$$

Similarly, summing moments about the connection joint c_{j-1} for the terminal link and equating to the time derivative of angular momentum in the j body frame yields

$$\mathbf{r}^{\,m}_j \times \mathbf{T}^j_I(\mathbf{F}_{Dj} + \mathbf{W}_j) + \mathbf{r}^c_j \times \mathbf{T}^j_I\mathbf{F}_T + \mathbf{T}^j_{j-1}\mathbf{L}_{j-1} = (\mathbf{I}_j\boldsymbol{\alpha}_{j/I} + \boldsymbol{\omega}_{j/I} \times \mathbf{I}_j\boldsymbol{\omega}_{j/I}) + \mathbf{r}^m_j \times m_j\mathbf{a}^m_j \tag{35}$$

The $\mathbf{i}$ component of both sides of the moment summation (35) reduce to zero, due to each link being a body of revolution and the fact that the position vector from connection joint $j-1$ to the mass center of the terminal link is defined such that it only has an $\mathbf{i}$ component. The remaining terminal link equations are assembled into a 5×1 force vector $\mathbf{F}_j$, arranged such that the first two equations represent the two nonzero components of the moment equation and the remaining

three equations are components of the force Eq. (34). The force vector takes the form

$$\mathbf{F}_j = \mathbf{M}_j \dot{\mathbf{v}}_j + \Gamma_T \tag{36}$$

where Eq. (29) is incorporated in to both Eqs. (34) and (35) with the following definitions:

$$\mathbf{F}_j = \begin{Bmatrix} 0 \\ \mathbf{R}_{j-1} \end{Bmatrix}, \qquad \mathbf{M}_j = \begin{bmatrix} \tilde{\mathbf{I}}_j - m_j \tilde{\mathbf{S}}_j^m \tilde{\mathbf{S}}_j^m & m_j \hat{\mathbf{S}}_j^m \mathbf{T}_{j-1}^j \\ m_j (\mathbf{T}_{j-1}^j)^T (\hat{\mathbf{S}}_j^m)^T & m_j \mathbf{E}_3 \end{bmatrix} \tag{37}$$

$$\tilde{\mathbf{I}}_j = \begin{bmatrix} I_{yy} & 0 \\ 0 & I_{zz} \end{bmatrix}, \qquad \tilde{\mathbf{S}}_j^m = \begin{bmatrix} 0 & -x_{mj} \\ x_{mj} & 0 \end{bmatrix}$$
$$\hat{\mathbf{S}}_j^m = \begin{bmatrix} 0 & 0 & -x_{mj} \\ 0 & x_{mj} & 0 \end{bmatrix} \tag{38}$$

z

$$\Gamma_T = \begin{bmatrix} -\hat{\mathbf{S}}_j^m \mathbf{T}_I^j (\mathbf{F}_{Dj} + \mathbf{W}_j) - \hat{\mathbf{S}}_j^c \mathbf{T}_I^j \mathbf{F}_T - \hat{\mathbf{T}}_{j-1}^j \tilde{\mathbf{L}}_{j-1} \\ m_j (\mathbf{T}_{j-1}^j)^T (\boldsymbol{\omega}_{j/I} \times (\boldsymbol{\omega}_{j/I} \times \mathbf{r}_j^m)) - \mathbf{T}_I^{j-1} (\mathbf{F}_{Dj} + \mathbf{W}_j + \mathbf{F}_T) \end{bmatrix} \tag{39}$$

The terms $\mathbf{r}_j^m \times m_j(\boldsymbol{\omega}_{j/I} \times (\boldsymbol{\omega}_{j/I} \times \mathbf{r}_j^m))$ and $\boldsymbol{\omega}_{j/I} \times \mathbf{I}_j \boldsymbol{\omega}_{j/I}$ from Eq. (35) vanish, due to the fact that the position vector from connection joint $j-1$ to the mass center of the terminal link is defined such that it only has only an $\mathbf{i}$ component, the links are bodies of revolution, and the spin rate in Eq. (18) is zero.

Substituting Eq. (31), the kinematic relationship for the acceleration vector $\dot{\mathbf{v}}_j$ into Eq. (36) gives a relationship for the force vector $\mathbf{F}_j$, in terms of the relative angular acceleration vector $\dot{\boldsymbol{\omega}}_j$, expressed as

$$\mathbf{F}_j = \mathbf{M}_j (\mathbf{D}_j \dot{\mathbf{v}}_{j-1} + \mathbf{G}_j \dot{\boldsymbol{\omega}}_j + \boldsymbol{\Lambda}_j) + \Gamma_T \tag{40}$$

The relative angular acceleration vector $\dot{\boldsymbol{\omega}}_j$ is then found by premultiplying Eq. (40) by $\mathbf{G}_j^T$ and noting that $\mathbf{G}_j^T \mathbf{F}_j = 0$:

$$\dot{\boldsymbol{\omega}}_j = -(\mathbf{G}_j^T \mathbf{M}_j \mathbf{G}_j)^{-1} \mathbf{G}_j^T (\mathbf{M}_j \mathbf{D}_j \dot{\mathbf{v}}_{j-1} + \mathbf{M}_j \boldsymbol{\Lambda}_j + \Gamma_T) \tag{41}$$

Substitution of Eqs. (31) and (41) into the force vector in Eq. (36) results in a final expression for the terminal body's force vector expressed only using its forces and the parent body's joint accelerations:

$$\mathbf{F}_j = \hat{\mathbf{M}}_j \mathbf{D}_j \dot{\mathbf{v}}_{j-1} + \hat{\Gamma}_j \tag{42}$$

where

$$\hat{\mathbf{M}}_j = \mathbf{M}_j - \mathbf{K}_j \mathbf{G}_j^T \mathbf{M}_j \tag{43}$$

$$\mathbf{K}_j = \mathbf{M}_j \mathbf{G}_j (\mathbf{G}_j^T \mathbf{M}_j \mathbf{G}_j)^{-1} \tag{44}$$

$$\hat{\Gamma}_j = \Gamma_j^a - \mathbf{K}_j \mathbf{G}_j^T \Gamma_j^a \tag{45}$$

$$\Gamma_j^a = \Gamma_T + \mathbf{M}_j \boldsymbol{\Lambda}_j \tag{46}$$

B. Nonterminal Body Recursive Dynamics

Following similar steps as outlined above for the terminal link, vector equations for the nonterminal links can be formed. Forces are summed on each of these links, and moments are summed about the (c_{j-1})th connection joint for each jth link in the tether. Again, the moment equations are expressed in the jth body frame, and the force equations are expressed in the $(j-1)$th body frame. All nonterminal links can be shown to have an equivalent recursive form,

$$\mathbf{R}_{j-1} - (\mathbf{T}_{j-1}^j)^T \mathbf{R}_j + \mathbf{T}_I^{j-1} (\mathbf{F}_{Dj} + \mathbf{W}_j) = m_j (\mathbf{T}_{j-1}^j)^T \mathbf{a}_j^m \tag{47}$$

by summing forces and equating to the time derivative of linear momentum. The moment equation then takes the form

$$\mathbf{r}_j^m \times \mathbf{T}_I^j (\mathbf{F}_{Dj} + \mathbf{W}_j) - \mathbf{r}_j^c \times \mathbf{R}_j + \mathbf{T}_{j-1}^j \mathbf{L}_{j-1} - \mathbf{L}_j = (\mathbf{I}_j \boldsymbol{\alpha}_{j/I} + \boldsymbol{\omega}_{j/I} \times \mathbf{I}_j \boldsymbol{\omega}_{j/I}) + \mathbf{r}_j^m \times m_j \mathbf{a}_j^m \tag{48}$$

Equations (47) and (48) may now be assembled into matrix form in a similar fashion to that of the terminal link. The $\mathbf{i}$ component of the moment equation vanishes and the matrix form reduces to a 5×1 system. Nonterminal links all have the equivalent form:

$$\mathbf{F}_j = \mathbf{M}_j \dot{\mathbf{v}}_j + \Gamma_j + \mathbf{D}_{j+1}^T \mathbf{F}_{j+1} \tag{49}$$

with

$$\Gamma_j = \begin{bmatrix} -\hat{\mathbf{S}}_j^m \mathbf{T}_I^j (\mathbf{F}_{Dj} + \mathbf{W}_j) - \hat{\mathbf{T}}_{j-1}^j \tilde{\mathbf{L}}_{j-1} + \tilde{\mathbf{L}}_j \\ m_j (\mathbf{T}_{j-1}^j)^T (\boldsymbol{\omega}_{j/I} \times (\boldsymbol{\omega}_{j/I} \times \mathbf{r}_j^m)) - \mathbf{T}_I^{j-1} (\mathbf{F}_{Dj} + \mathbf{W}_j) \end{bmatrix} \tag{50}$$

where the terms $\mathbf{r}_j^m \times m_j(\boldsymbol{\omega}_{j/I} \times (\boldsymbol{\omega}_{j/I} \times \mathbf{r}_j^m))$ and $\boldsymbol{\omega}_{j/I} \times \mathbf{I}_j \boldsymbol{\omega}_{j/I}$ become zero just as with the terminal link. The force vector (49) for the jth body is coupled to the force vector from the previous link by the term $\mathbf{D}_{j+1}^T \mathbf{F}_{j+1}$. It can be shown that the force vector for any nonterminal link can be written just as the terminal link (42), where it depends on its forces and the parent body's joint accelerations. Substitution of the terminal link force vector (42) into Eq. (49) results in

$$\mathbf{F}_j = \tilde{\mathbf{M}}_j \dot{\mathbf{v}}_j + \tilde{\Gamma}_j \tag{51}$$

where

$$\tilde{\mathbf{M}}_j = \mathbf{M}_j + \mathbf{D}_{j+1}^T \hat{\mathbf{M}}_{j+1} \mathbf{D}_{j+1} \tag{52}$$

$$\tilde{\Gamma}_j = \Gamma_j + \mathbf{D}_{j+1}^T \hat{\Gamma}_{j+1} \tag{53}$$

Substitution of Eq. (31) into Eq. (51) gives a relationship for the force vector $\mathbf{F}_j$, in terms of the relative angular acceleration vector $\dot{\boldsymbol{\omega}}_j$. As with the terminal link, first multiplying by $\mathbf{G}_j^T$ and noting that $\mathbf{G}_j^T \mathbf{F}_j = 0$, results in $\dot{\boldsymbol{\omega}}_j$ for nonterminal links taking the form

$$\dot{\boldsymbol{\omega}}_j = -(\mathbf{G}_j^T \tilde{\mathbf{M}}_j \mathbf{G}_j)^{-1} \mathbf{G}_j^T (\tilde{\mathbf{M}}_j \mathbf{D}_j \dot{\mathbf{v}}_{j-1} + \Gamma_j^a) \tag{54}$$

where

$$\Gamma_j^a = \tilde{\Gamma}_j + \tilde{\mathbf{M}}_j \boldsymbol{\Lambda}_j \tag{55}$$

The nonterminal link force vector then takes the form

$$\mathbf{F}_j = \hat{\mathbf{M}}_j \mathbf{D}_j \dot{\mathbf{v}}_{j-1} + \hat{\Gamma}_j \tag{56}$$

by combining Eqs. (31) and (54) with Eq. (51) and defining

$$\hat{\mathbf{M}}_j = \tilde{\mathbf{M}}_j - \mathbf{K}_j \mathbf{G}_j^T \tilde{\mathbf{M}}_j \tag{57}$$

$$\mathbf{K}_j = \tilde{\mathbf{M}}_j \mathbf{G}_j (\mathbf{G}_j^T \tilde{\mathbf{M}}_j \mathbf{G}_j)^{-1} \tag{58}$$

$$\hat{\Gamma}_j = \Gamma_j + \tilde{\mathbf{M}}_j \boldsymbol{\Lambda}_j - \mathbf{K}_j \mathbf{G}_j^T \Gamma_j^a \tag{59}$$

C. Solution Procedure

The recursive solution begins with a backward pass through the tether system, starting at the terminal link. At the terminal link ($j = N$) the force vector, $\mathbf{F}_j$ in Eqs. (36) and (42) can be formed. Formation of force vectors for all nonterminal links then follows for $j = N - 1$ to 1 using Eqs. (51) and (56). Upon reaching the root link ($j = 1$), the acceleration vector $\dot{\mathbf{v}}_1$ in Eq. (51) becomes solvable. Since the root link is attached to the ground, $\mathbf{a}_0^c$ is zero and the solution to $\tilde{\boldsymbol{\alpha}}_{1/I}$ only requires the inversion of a 2×2 matrix. Therefore, at the end of the backwards pass, the solution to $\dot{\mathbf{v}}_1$ is found. Once the acceleration vector $\dot{\mathbf{v}}_1$ for the root link is known, a forward pass is used to find the angular acceleration vector $\dot{\boldsymbol{\omega}}_j$ and the acceleration vector $\dot{\mathbf{v}}_j$, using Eqs. (31) and (54) for $j = 2$ to $N - 1$, then Eqs. (31) and (41) for $j = N$. Completion of the forward pass results in the solution to the N angular accelerations $\tilde{\boldsymbol{\alpha}}_{j/I}$, for $j = 1$ to N, required for numerical integration.

V. Simulations

A. System Parameters

To demonstrate application of the proposed model and its utility in analyzing the aerostat and tether dynamics along with tether loads, simulations of an example 17 m aerostat, similar to that used in the RAID system, is evaluated with a 250 m of tether. Characteristics of the aerostat are provided in Table 1. The tether has a 7 mm diameter and a total mass of 23 kg and is divided into 11 segments, with a joint damping coefficient of 46 N · s. The viscoelastic element has an unstretched length L_{ve} of 10 m and K_s, K_v, and C_v of 575 N/m, 3100 N/m, and 350 N · s/m, respectively.

B. System Response Because of Varying Wind Speed and Direction

In the first simulation, the aerostat is initially directly above the ground connection with no wind and the tether vertical. Orientation of the aerostat is initially facing in the opposite direction of $\mathbf{i}_I$, with ψ_B being π. Wind conditions for the simulation are such that the wind is increased from 0 to 10 m/s over a 10 s interval, with a direction of 15 deg. During the period between 90 and 100 s, the wind rotates to −15 deg while also increasing to 15 m/s. Wind conditions are depicted in Fig. 2. Aerostat, viscoelastic, and recursive tether differential equations are numerically integrated using a fourth-order Runge–Kutta algorithm with a time step of 0.05 s.

The displacement response of the aerostat due to the specified wind parameters is shown by side and top views in Figs. 3 and 4. The range and altitude displacement at $t = 0$, 90, and 200 s are shown in Fig. 3, and range and cross-range displacement (also at $t = 0$, 90, and 200 s) are shown in Fig. 4. The altitude of the aerostat decreases from an initial height of 260 m to approximately 252 m over the first 90 s of the simulation, while the aerostat moves approximately 50 m in the horizontal direction. Altitude eventually decreases to 240 m, and the horizontal displacement reaches a final value of 120 m as the wind increases.

Table 1 Aerostat parameters

Parameter	Value	Units
Vol	290	m^3
m	180	kg
A	41.8	kg
B	279	kg
Q	4162	kg · m^2
I_{xx}	310	kg · m^2
I_{yy}, I_{zz}	1455	kg · m^2
C_{A0}	−0.04	——
C_{A2}	0.002	——
$C_{Y\beta}$	−0.06	——
C_{AN}	−0.03	——
C_{lp}	−0.005	——
C_{nr}, C_{mq}	−0.03	——
C_{m0}	0.02	——
$C_{m\alpha}$, $C_{n\beta}$	−0.07	——

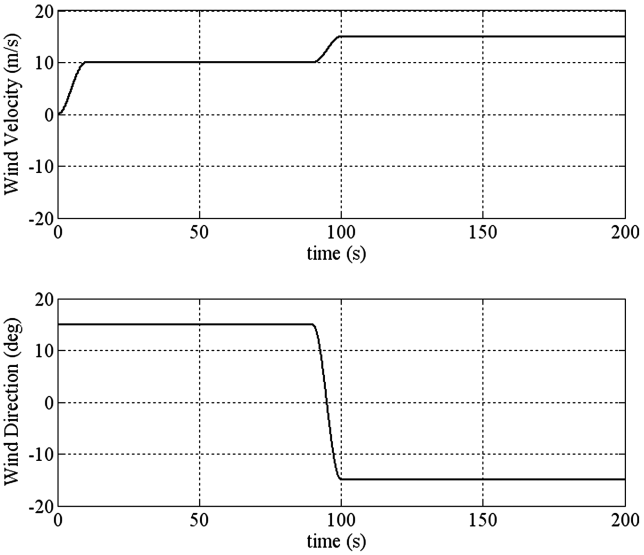

Fig. 2 Wind conditions for initial aerostat simulation.

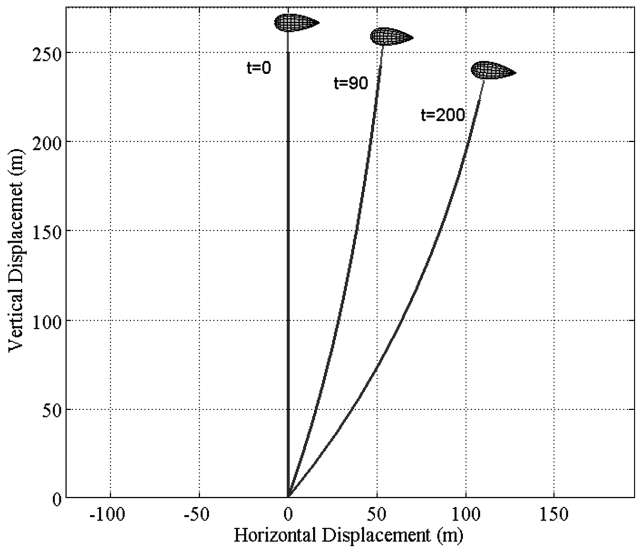

Fig. 3 Simulated aerostat vertical-plane response.

The tether tension force in the viscoelastic element is shown in Fig. 5. Initially, the tension force oscillates in the first 30 s, with a peak value of approximately 768 N. As the wind conditions remain constant, the tension begins to approach a steady-state value of 710 N. Once the wind changes direction, a similar oscillatory response is seen between 90 and 140 s, and the tension force peaks at a value of 803 N. As the simulation progresses and the wind conditions again remain constant, a steady-state value of 740 N in the viscoelastic element is eventually reached.

Aerostat yaw, pitch, and roll angles are shown in Fig. 6, and the total velocity of the aerostat is shown in Fig. 7. The roll angle shows little change through the simulation; however, a noticeable response is noted to occur when the wind changes direction at $t = 90$ s. Similarly, pitching dynamics of the aerostat are most significant after wind changes. In response to increasing winds and increasing tether drag, the steady-state aerostat pitch angle increases to maintain equilibrium. As earlier noted, the aerostat has an initial yaw angle of 180 deg. It oscillates during the first 50 s and appears to be reaching a steady-state value of 195 deg until the change in the wind conditions at 90 s. A similar oscillatory response is noted before a steady-state value of 165 deg for the yaw angle is attained. Aerostat total velocity is shown in Fig. 7. in which the maximum velocity of 4.7 m/s occurs

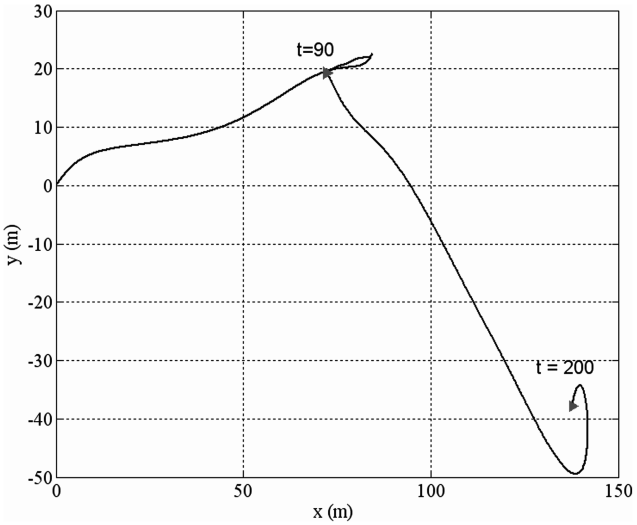

Fig. 4 Aerostat horizontal-plane displacement.

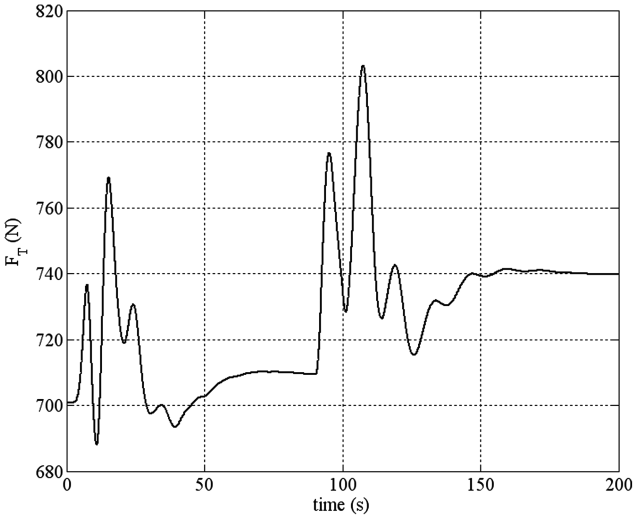

Fig. 5 Tension in viscoelastic element.

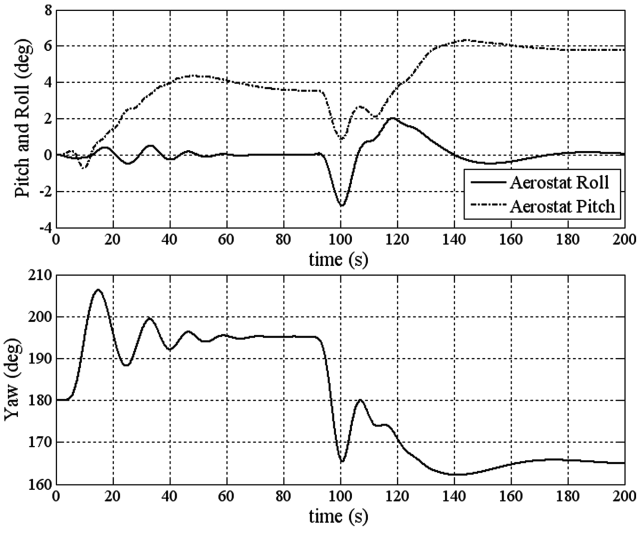

Fig. 6 Aerostat roll, pitch, and yaw angles.

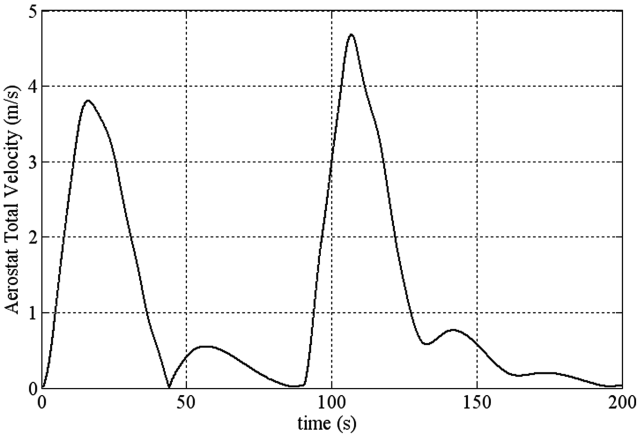

Fig. 7 Aerostat total velocity.

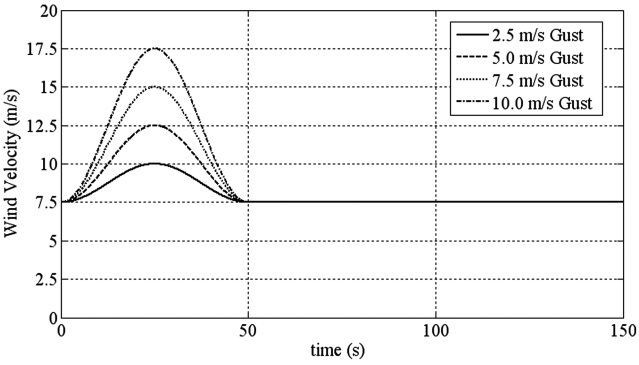

Fig. 8 Wind conditions with increasing gusts of 2.5 m/s.

at approximately 105 s. The total aerostat velocity eventually approaches zero, as the wind conditions remain at constant values through the remaining portion of the simulation.

C. System Response Because of Simulated Wind Gusts

An investigation of the effects from wind gusts on the aerostat is shown using multiple simulations of the proposed model under different conditions. Initially the tethered aerostat system is at equilibrium in a 7.5 m/s wind from 0.0 deg with ψ_B being π. Wind gusts were simulated by superimposing a 50 s sinusoidal gust, also at 0.0 deg, in addition to the 7.5 m/s constant wind. Four cases were simulated with gusts of an additional 2.5, 5.0, 7.5, and 10 m/s,

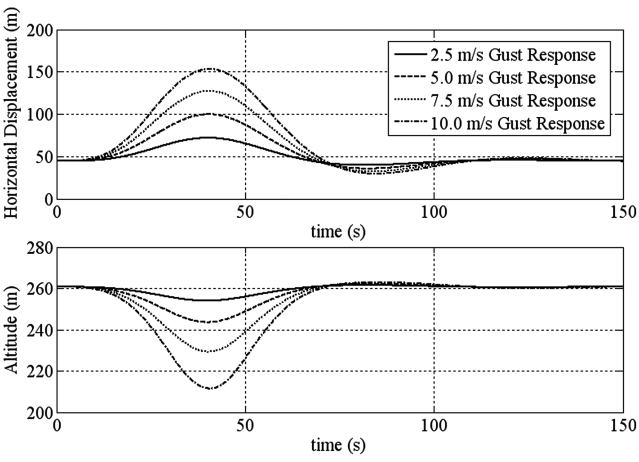

Fig. 9 Aerostat horizontal displacement and altitude.

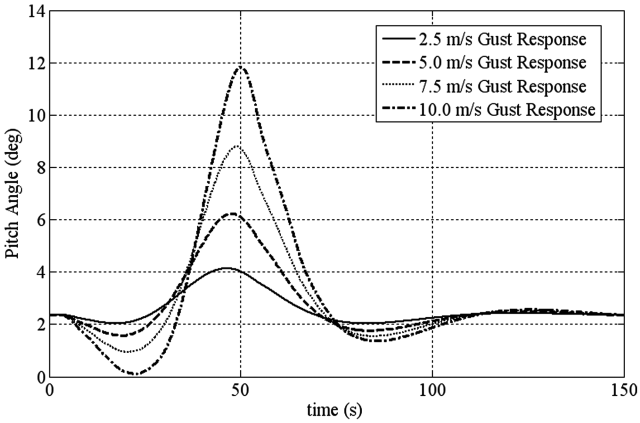

Fig. 10 Aerostat pitch angle.

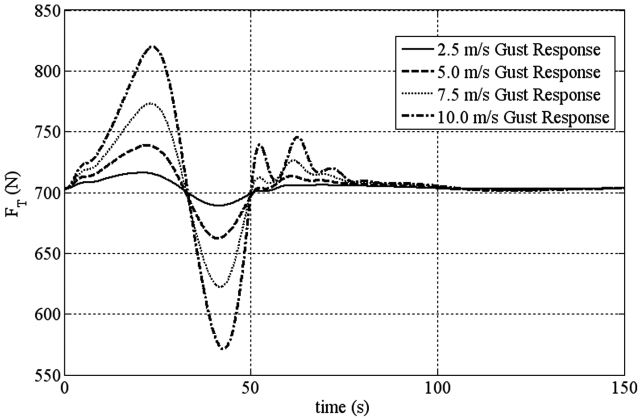

Fig. 11 Tension in viscoelastic element.

respectively, after which the wind speed remained constant at its initial value of 7.5 m/s, as shown in Fig. 8.

The altitude and horizontal displacement of the aerostat are shown in Fig. 9. For each simulation, the horizontal displacement reaches a maximum value at $t = 40$ s, with the maximum displacement of approximately 150 m occurring as a result of the 10 m/s wind gust. The altitude decreases as the wind gusts increase, and the minimum value recorded for the 10 m/s gust is about 212 m. Both the horizontal displacement and altitude converge on a steady-state value as the wind speed drops back to a constant value of 7.5 m/s. Figure 10 shows the pitch angles all initially at 2.4 deg, with a maximum pitch achieved for each just after the gust ends. The maximum value of 11.9 deg is noted in the 10 m/s case at $t = 50$ s. The 2.5, 5.0, and 7.5 m/s gust simulations produce maximum pith angles of 4.1, 6.2, and 8.8 deg at times of 47, 48, and 49 s, respectively.

The tension in the viscoelastic element from each gust is shown in Fig. 11. In all cases the maximum tension occurs as the gust reaches its largest value, after which the tension decrease dramatically as the aerostat surges forward after the gust in over. Tether tension at the aerostat is highly dependent on the gust magnitude, with the maximum tension of 820 N appearing in the case of the 10 m/s gust at a time of 25 s, which is the peak of the wind gust. The minimum tensions occurs at $t = 40$ s, which is 575 N after the 10 m/s gust. All four cases eventually converge on a tension of 700 N as the winds once again become constant after their initial gusts.

VI. Conclusions

A computationally efficient tethered aerostat model was developed by coupling a discrete model for low-strain tethers and a conventional six-degree-of-freedom aerostat model with a single viscoelastic element. The recursive tether model was based on a joint-coordinate formulation, resulting in a set of unconstrained differential equations. Each link is treated as a body of revolution and it is assumed that tether spin was negligible to the dynamics, resulting in each link having only two degrees of freedom. An order-N recursive algorithm for the tether dynamics was then developed in order to maintain computational efficiency as the number of bodies N increased. An advantage of the proposed method is the absence of high-frequency axial vibration, allowing larger integration time steps, further improving computation speeds. The result is a computationally efficient model that can accurately represent a low-strain tether (used in many engineering applications) without the need to add stiff elastic elements. A specific application was then presented which consisted of a 17 m aerostat similar to that used in the RAID system connected to 250 m tether. The efficiency and effectiveness of the proposed tethered aerostat system was demonstrated through a single simulation with changing winds and later by a set of simulations investigating the response to wind gusts of varying magnitude.

References

[1] Schmidt, D. K., "Modeling and Near-Space Stationkeeping Control of a Large High-Altitude Airship," *Journal of Guidance, Control, and Dynamics*, Vol. 30, No. 2, 2007, pp. 540–547. doi:10.2514/1.24865

[2] Li, Y., and Nahon, M., "Modeling and Simulation of Airship Dynamics," *Journal of Guidance, Control, and Dynamics*, Vol. 30, No. 6, 2007, pp. 1691–1700. doi:10.2514/1.29061

[3] Lee, S., and Bang, H., "Three-Dimensional Ascent Trajectory Optimization for Stratospheric Airship Platforms in the Jet Stream," *Journal of Guidance, Control, and Dynamics*, Vol. 30, No. 5, 2007, pp. 1341–1352. doi:10.2514/1.27344

[4] Slegers, N., and Brown, A. X., "Comment on Three-Dimensional Ascent Trajectory Optimization for Stratospheric Airship Platforms in the Jet Stream," *Journal of Guidance, Control, and Dynamics*, Vol. 32, No. 5, 2009, pp. 1692–1693. doi:10.2514/1.45171

[5] Kang, W., and Lee, I., "Analysis of tethered Aerostat Response Under Atmospheric Turbulence Considering nonlinear Cable Dynamics," *Journal of Aircraft*, Vol. 46, No. 1, 2009, pp. 343–347. doi:10.2514/1.38599

[6] Aglietti, G., "Dynamic Response of a High-Altitude Tethered Balloon System," *Journal of Aircraft*, Vol. 46, No. 6, 2009, pp. 2032–2040. doi:10.2514/1.43332

[7] Nahon, M., Gilardi, G., and Lambert, C., "Dynamics/Control of a Radio Telescope Receiver Supported by a Tethered Aerostat," *Journal of Guidance, Control, and Dynamics*, Vol. 25, No. 6, 2002, pp. 1107–1115. doi:10.2514/2.4990

[8] Lambert, C., Nahon, M., Chalmers, D., and Gilardi, G., "Cable Control of an Aerostat Platform: Experimental Results and Model Validation," *Journal of Guidance, Control, and Dynamics*, Vol. 30, No. 2, 2007, pp. 620–628. doi:10.2514/1.22598

[9] Frost, G., and Costello, M., "Improved Deployment Characteristics of a Tether-Connected Munition System," *Journal of Guidance, Control, and Dynamics*, Vol. 24, No. 3, 2001, pp. 547–554. doi:10.2514/2.4745

[10] Kyle, J., and Costello, M., "Comparison of Measured and Simulated Motion of a Scaled Dragline Excavation System," *Mathematical and Computer Modelling*, Vol. 44, No. 9–10, 2006, pp. 816–833. doi:10.1016/j.mcm.2006.02.015

[11] Jerkovsky, W., "The Structure of Multibody Dynamic Equations," *Journal of Guidance, Control, and Dynamics*, Vol. 1, No. 3, 1978, pp. 173–182. doi:10.2514/3.55761

[12] Kane, T., Linkins, P., and Levinson, D., *Spacecraft Dynamics*, McGraw–Hill, New York, 1983.

[13] Hollerbach, J., "A Recursive Lagrangian Formulation of Manipulator Dynamics and a Comparative Study of Dynamic Formulation Complexity," *IEEE Transactions on Systems, Man, and, Cybernetics*, Vol. 10, No. 11, 1980, pp. 730–736.

doi:10.1109/TSMC.1980.4308393
[14] Schielen, W., "Computational Dynamics: Theory and Application of Multibody Systems," *European Journal of Mechanics, A/Solids*, Vol. 25, 2006, pp. 566–594. doi:10.1016/j.euromechsol.2006.03.004
[15] Hembree, B., and Slegers, N., "Efficient Tether Dynamic Model Formulation Using Recursive Rigid-Body Dynamics," *Proceedings of the Institution of Mechanical Engineers, Part K (Journal of Multi-Body Dynamics)*, Vol. 224, 2010. doi:10.1243/14644193JMBD255
[16] Kuipers, J., *Quaternions and Rotation Sequences*, Princeton Univ. Press, Princeton, NJ, 1999, pp. 103–136.
[17] Lissaman, P., and Brown, G., "Apparent Mass Effects on Parafoil Dynamics," AIAA Paper 93-1236, May 1993.
[18] Lamb, H., *Hydrodynamics*, Dover, New York, 1945, pp. 160–174.
[19] Khoury, G. H., and Gillet, J. D., *Airship Technology*, Cambridge Univ. Press, Cambridge, England, U.K., 1999.